Research Square

Preprints are preliminary reports that have not undergone peer review.
They should not be considered conclusive, used to inform clinical practice,
or referenced by the media as validated information.

Hydrothermally Synthesized BiOI/MWCNT Composite Flexible Thin Films for High-Performance Solid-State Supercapacitors

Nashiruddin Ahammed
Presidency University
Sukanta De
sukanta.physics@presiuniv.ac.in
Presidency University

Research Article

Keywords: Thin film, Flexible, Nanomaterials, BiOI nanoplate, Supercapacitor

Posted Date: November 17th, 2026

DOI: https://doi.org/10.21203/rs.3.rs-11362863/v1

License: This work is licensed under a Creative Commons Attribution 4.0 International License.
Read Full License

Additional Declarations: No competing interests reported.

Hydrothermally Synthesized BiOI/MWCNT Composite Flexible Thin Films for High-Performance Solid-State Supercapacitors

Nashiruddin Ahammed[1,2] and Sukanta De[1]

[1]*Department of Physics, Presidency University, 86/1 College Street, Kolkata-700073, India*
[2]*Department of Physics, Government General Degree College Nakashipara, Muragachha, Nadia-741154, India.*

[*]Corresponding Author E-mail: sukanta.physics@presiuniv.ac.in

Abstract: High-surface-area two-dimensional (2D) bismuth oxyiodide (BiOI) nanoplatelets with abundant electroactive sites were synthesized using a simple and cost-effective hydrothermal method. Flexible BiOI/multiwalled carbon nanotube (MWCNT) composite thin films with varying weight percentages of BiOI and MWCNT were fabricated and evaluated for their electrochemical performance in a symmetric two-electrode configuration. Among the prepared composites, the film with a BiOI-to-MWCNT mass ratio of 60:40 exhibited superior electrochemical performance, delivering a specific capacitance of 218 F g^{-1} and an energy density of 7.6 Wh kg^{-1} at a power density of 0.136 kW kg^{-1}, using a PVA/H_2SO_4 gel as the solid-state electrolyte. The fabricated flexible solid-state supercapacitor device (FSSSD60) demonstrated excellent cycling stability, retaining 95% of its initial specific capacitance after 10,000 charge–discharge cycles. Furthermore, the device exhibited excellent mechanical flexibility, maintaining nearly constant electrochemical performance when bent at different angles. These results highlight the potential of BiOI/MWCNT composite thin films as promising electrode materials for flexible, high-performance solid-state supercapacitors.

Keywords: Thin film, Flexible, Nanomaterials, BiOI nanoplate , Supercapacitor.

1. Introduction:

The persistent exhaustion of global fossil fuel reserves and rising greenhouse gas emissions have pivoted the global research focus toward renewable energy sources such as wind, solar, ocean, water and biomass which expedites the shift toward a carbon-neutral and sustainable development model. The high-performance storage systems characterized by superior energy and power densities along with extended cyclic stability are required for the efficient utilization of renewable energy [1-4]. The rapid adoption of electric vehicles and integrated smart grids, alongside the rising popularity of flexible and wearable electronic devices underscore the urgent need for high-performance power sources [5-6]. Although lithium ion batteries offer superior energy density for portable devices, their sluggish charge transfer kinetics and limited cycle life compel to develop the alternative systems, such as supercapacitors, which provide exceptional power delivery and durability and fulfil the operational performance criteria for electric vehicle acceleration and braking [7-9].

A supercapacitor, also known as an ultracapacitor, is an electrochemical energy storage device that bridges the performance gap between conventional capacitors (high power, low energy) and rechargeable batteries (low power, high energy). Unlike batteries, which rely on slow, bulk chemical reactions, supercapacitors store charge primarily through interfacial charge storage mechanisms, where energy is stored through ion accumulation or fast redox reactions at the electrode-electrolyte interface [10-11].

Supercapacitors store energy through two primary mechanisms: Electric Double-Layer Capacitance (EDLC) and pseudo capacitance, which are often combined in hybrid capacitors. In an EDLC, energy is stored electrostatically through the reversible adsorption of ions at the electrode-electrolyte interface, typically using high-surface-area carbon materials like MWCNTs [12-13]. Conversely, pseudocapacitance involves fast, reversible Faradaic redox reactions occurring at or near the electrode surface, a characteristic common in transition metal oxides (like Bi_2O_3, Nb_2O_5, TiO_2 , V_2O_5 , MnO_2 , NiO, Co_3O_4) [14-15] ; transition metal

oxychloride (FeOCl, CrOCl) [16-17] , metal hydroxide (Nickel Hydroxide $Ni(OH)_2$; Cobalt Hydroxide $Co(OH)_2$) [18], metal nitrides (TiN, VN) [19] ; composite materials ($BaSnO_3$/rGO Nanocomposites, MnO_2/graphene, Fe_3O_4/carbon) [20-21] and conducting polymers (epolyaniline, polypyrrole) [22].

Two-dimensional (2D) materials have emerged as transformative candidates for high-performance supercapacitors due to their unique structural and electrochemical properties. Their planar architecture provides a high surface-to-volume ratio, exposing an abundance of electroactive sites that facilitate rapid interfacial charge storage. Furthermore, the atomic-scale thickness of 2D nanostructures significantly shortens ion diffusion paths, ensuring superior charge-transfer kinetics compared to bulk materials. However, the practical application of pure 2D semiconductors is often hindered by limited electronic conductivity and the tendency of nanosheets to restack, which reduces the effective surface area [23-26].
To circumvent these limitations, the fabrication of a heterostructure incorporating Multi-Walled Carbon Nanotubes (MWCNTs) offers a highly effective strategy. In this composite framework, the MWCNTs act as a sophisticated conductive network, providing continuous paths that bolster long-range electron transport. Beyond enhancing conductivity, the MWCNTs function as intercalants to inhibit the aggregation of 2D layers, preserving the high surface area and accessible porosity of the electrode. This synergistic integration reconciles the trade-off between surface area and conductivity, resulting in a hierarchical architecture with optimized internal resistance and enhanced cyclic stability for next-generation energy storage [27-28].

However, the development of flexible, high-performance electrodes is a critical frontier in energy storage, requiring a synergistic integration of redox-active species and conductive carbonaceous scaffolds. Two-dimensional (2D) materials, such as Bi_2O_3, MoS_2, and V_2O_5, are highly advantageous for these systems due to their abundant electroactive surface area and shortened ion-diffusion pathways. When coupled with Multi-Walled Carbon Nanotubes (MWCNTs) or graphene, these hybrids demonstrate exceptional mechanical resilience and rate capability [29-32]. The carbonaceous components serve a dual role: they function as a continuous conductive network that bypasses the high intrinsic resistance of semiconducting oxides and act as structural scaffolding that obstructs the deleterious restacking of 2D nanosheets during electrode assembly. In contrast, several technical drawbacks persist in the practical deployment of these flexible architectures. While materials like carbon cloth or MWCNT provide a robust physical substrate, the interfacial adhesion between the active 2D

nanoplates and the flexible carbon network is often weak, leading to material delamination and a subsequent rise in equivalent series resistance (ESR) during repeated mechanical deformation [33-35]. Furthermore, balancing the mass loading of the active material with the weight of the carbonaceous support is essential to minimize electrochemically inactive volume, which can compromise the overall volumetric energy density. Addressing these interfacial and kinetic limitations through advanced nanocomposite engineering remains paramount for the development of next-generation wearable energy storage devices [36-37].

Conductive polymers like polyaniline (PANI) provide high capacitance through Faradaic mechanisms but suffer from mechanical degradation due to repeated swelling and shrinking. Hybridizing these polymers with a flexible MWCNT can enhance their cyclic stability by providing a robust mechanical scaffold [38-39]. Ultimately, the choice of the 2D species like a stable oxyiodide (BiOI) balances with a compatible carbonaceous support to ensure optimized energy density, power delivery, and long-term durability in flexible energy storage applications.

In this research work, we demonstrated the fabrication of a high-performance, flexible solid-state symmetric supercapacitor device (FSSSD) using a BiOI nanoplates/MWCNTs hybrids. The active electrodes, comprising hydrothermally synthesized BiOI nanoplates integrated with varying weight percentages of MWCNTs. The prepared composites were subsequently transferred onto polyethylene terephthalate (PET) substrates to facilitate mechanical flexibility of the thin film. Single-walled carbon nanotubes (SWCNTs) were used as current collectors instead of metal to make the device lighter and more flexible.

2. Experimental section

2.1 Chemicals

Bismuth nitrate pentahydrate [$Bi(NO_3)_3$, $5H_2O$)], potassium iodide (KI) and Polyvinyl alcohol (PVA) were procured from Sigma Aldrich. Multiwall carbon nanotubes (Length: 5-15nm, outer diameter: 60-100 nm) were acquired from io-Il-Tech nanomaterials. Sulfuric Acid (H_2SO_4, 98%) , sodium dodecyl sulfate (SDS, >90%), ammonia solution 25% were obtained from Merck Specialities Pvt. Ltd. All reagents were of analytical grade and used as received without further purification.

2.2 Synthesis protocol: BiOI Nanoplates

Bismuth oxyiodide (BiOI) nanoplates were synthesized via a hydrothermal method [40-41]. 4 mmol of bismuth nitrate pentahydrate [$Bi(NO_3)_3$, $5H_2O$] and 4 mmol of potassium iodide (KI) were successively dissolved in 60 mL of deionized water under vigorous magnetic stirring at room temperature. Ammonia solution was added dropwise to adjust the pH to approximately 6.0, followed by additional stirring for 1 h. This precursor solution was transferred into a 75 mL Teflon-lined autoclave, which was heated to 200 °C and held for 24 h. Post-reaction, the autoclave was allowed to air-cooled to room temperature. The products were centrifuged, washed with ethanol and DI water several times, then dried in an oven at 65 °C.

2.3 CNT dispersion and preparation of BiOI/MWCNT composite thin films

SDS stock solutions (5 mg mL^{-1} in deionized water) were obtained by overnight stirring under magnetic stirring at room temperature. Subsequently, stable CNT dispersions were prepared using SDS:CNT = 5:1 (w/w) via a three-stage sonication protocol: high-power ultrasonication (5 min), low-power ultrasonic bath (60 min), and high-power ultrasonication (5 min) followed by 24h stabilization. Dispersions were centrifuged at 6000 rpm for 90 min. Finally, supernatants were carefully collected for subsequent applications. The method was employed for both SWCNT and MWCNT dispersions [42].

BiOI nanoplates (1 mg mL^{-1} in ethanol) were dispersed via low-power bath sonication for 5 min, then combined with MWCNT dispersions at varying weight ratios. The mixtures were vacuum-filtered onto masked cellulose membranes to form thin films, which were dried in situ with the filtration assembly undisturbed. Prior to SWCNT thin film deposition by vacuum

filtration, the masking was removed from the BiOCl/MWCNT substrate. Subsequently, films were washed multiple times with DI water and transferred to flexible PET substrates as per reported protocol.

2.4 Preparation of PVA/H_2SO_4 Gel Electrolyte and electrode:

A homogeneous clear PVA solution was obtained by dissolving 1 g PVA in 10 mL DI water with stirring at 80 °C, after which 1 g H_2SO_4 was incorporated under vigorous stirring for 30 min to form the gel electrolyte.

Both cathode and anode comprised symmetric, equal-mass of BiOI/MWCNT thin films on PET substrates, employing PVA/H_2SO_4 gel as the solid electrolyte, wherein SWCNT networks served as current collectors. The Flexible solid-state symmetric supercapacitor device (FSSSD) with BiOI:MWCNTs mass ratios of 0:100, 20:80, 40:80, 60:40, 80:20 and 100:0 were designated as $FSSSD_0$, $FSSSD_{20}$, $FSSSD_{40}$, $FSSSD_{60}$, $FSSSD_{80}$ and $FSSSD_{100}$ respectively.

2.5 Characterization:

The crystal structure of pristine BiOI was investigated via X-ray diffraction (XRD) using a Bruker D8 Advance diffractometer with Cu K_α radiation (λ = 1.5418 Å) over 2θ = 20°–80°. Morphological characterization of the samples were performed using a scanning electron microscope (ZEISS GeminiSEM 450) equipped with EDX and the transmission electron microscope (TEM) images were recorded using JEOL JEM-2100 system. Raman scattering measurements were conducted on a Renishaw Micro Raman Spectrometer (UK) to evaluate the fundamental vibrational characteristics. The textural properties, including specific surface area and pore size distribution, were quantified via N_2 adsorption-desorption isotherms at 77 K using a BELSORP-max II instrument (Microtrac BEL Corp). The oxidation states and elemental purity of the synthesized products were scrutinized using AXIS Supra with monochromatic Al K_α X-ray source.

3 Result and discussion:

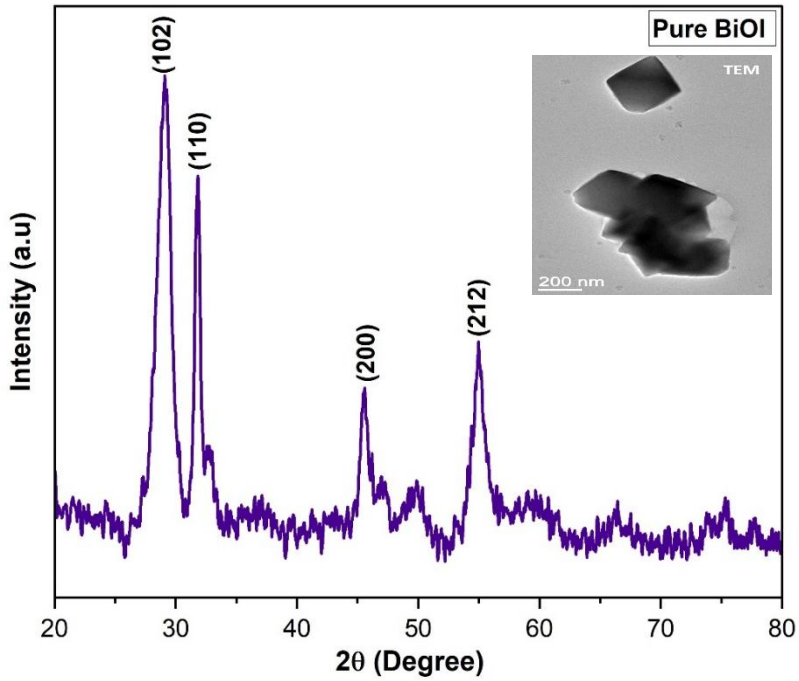


Figure 1: *XRD patterns of the pure BiOI nanoplate and inset TEM image of Pure BiOI nanoplate.*

The crystalline structure and phase purity of the as-synthesized BiOI nanomaterials were investigated using X-ray powder diffraction. The XRD pattern of the sample (***Figure 1***) exhibits sharp and well-defined diffraction peaks, indicating a high degree of crystallinity. All observed reflections can be indexed to the tetragonal phase of BiOI with the space group P_4/nmm, showing excellent agreement with the standard JCPDS card no. 73-2062 [43-44]. Specifically, the characteristic peaks observed at 2θ values of approximately 29.7°, 31.7°, 45.4°, and 55.2° correspond to the (102), (110), (200), and (212) crystallographic planes, respectively [45]. A notable feature of the BiOI nanoplate XRD pattern is the $I_{(110)}/I_{(102)}$ intensity ratio (0.78), which is higher than the standard 0.22 reported in JCPDS no. 73-2062. Such an enhancement confirms the preferential growth and exposure of {110} facets [46-47]. These facets play a critical role in optimizing electrochemical performance; by offering shortened diffusion channels and increasing the availability of active sites, they facilitate faster kinetics than standard microspheres. This structural orientation likely explains the superior rate capability observed during testing. The morphological features and structural integrity of the

BiOI samples were further investigated using Transmission Electron Microscopy (TEM). As illustrated in the inset of ***Figure 1***, the BiOI nanomaterial primarily consists of distinct nanoplate or nanosheet-like structure. The nanoplates exhibit high crystallinity and growth along specific crystallographic planes. These observations correlate well with the XRD results, where the high intensity of the {110} facets suggested a preferred orientation. The relatively smooth surfaces and well-defined edges of the plates are critical for electrochemical applications, as they maximize the exposure of active sites and provide unobstructed pathways for electrolyte ion diffusion.

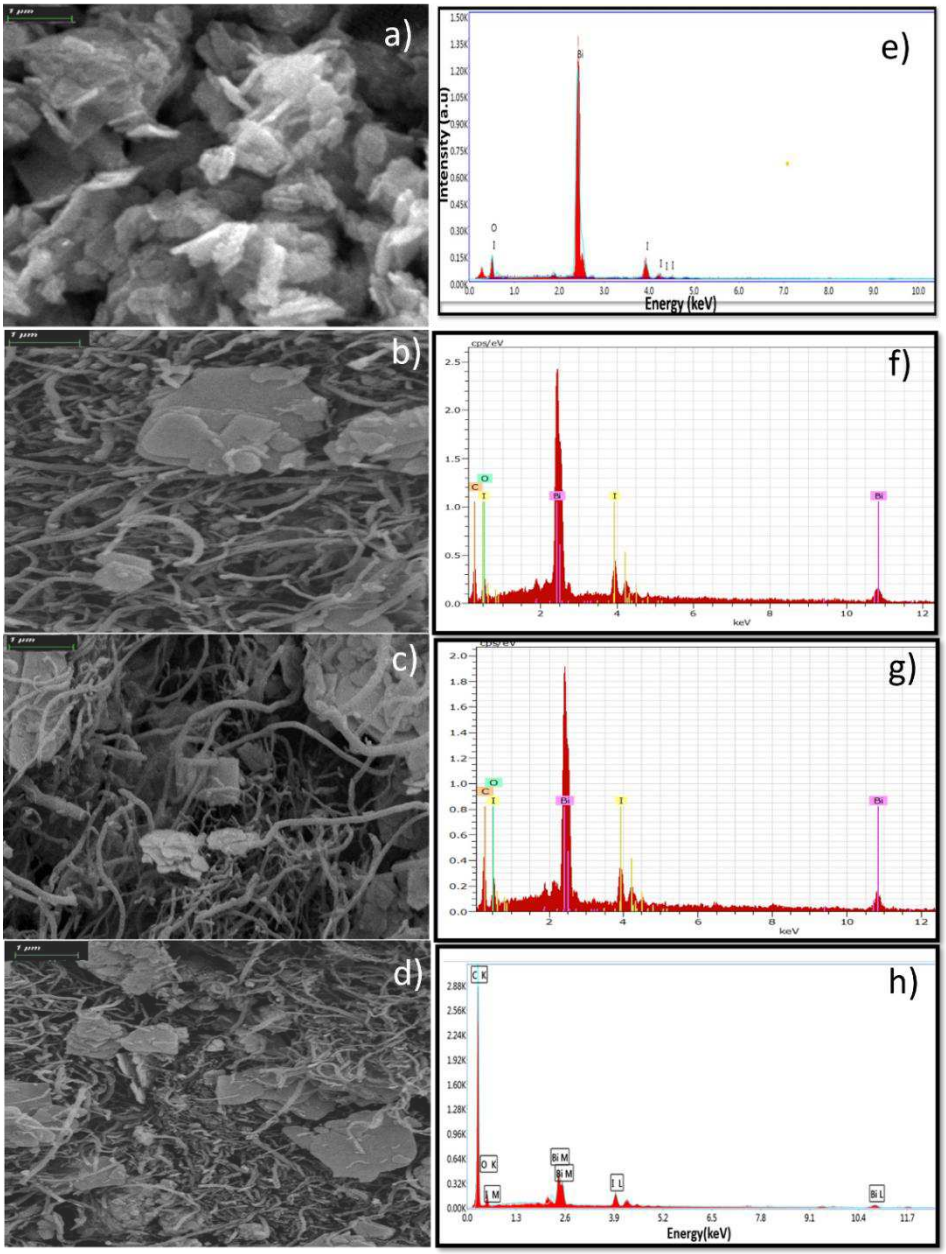


Figure 2*: SEM images of a) Pure BiOI nanoplate b) FSSSD$_{40}$ (c) FSSSD$_{60}$ d) FSSSD$_{80}$ and EDAX of e) Pure BiOI nanoplate f) FSSSD$_{40}$ g) FSSSD$_{60}$ h) FSSSD$_{80}$.*

The micrograph of the pure BiOI sample in ***Figure 2(a)*** reveals a well-defined nanoplate-based morphology. These 2D nanostructures exhibit distinct edges and smooth surfaces, consistent with the high degree of crystallinity previously inferred from XRD analysis. The discrete nature of these nanoplates is advantageous for maximizing the electrochemically active surface area. Upon the integration of MWCNTs, a significant morphological transition is observed ***Figure (2b-d)***. The FESEM images of the FSSSD series demonstrate a hierarchical hybrid architecture where the BiOI nanoplates are intimately anchored onto the entangled MWCNT network. In this configuration, the MWCNTs serve as conductive intercalants and structural pillars, effectively preventing the self-aggregation or restacking of the BiOI nanoplates. This interconnected framework facilitates rapid charge kinetics by providing continuous pathways for electron transport and ensuring efficient electrolyte infiltration throughout the electrode matrix. The electrochemical efficacy of these hybrids is critically governed by the BiOI-to-MWCNT mass ratio, which dictates the balance between conductivity and redox activity.
The MWCNT network is dominant in ***Figure 2 (b)***. While the electrical conductivity is high, the lower density of the pseudocapacitive BiOI nanoplates results in a deficit of redox-active sites. The specimen of ***Figure 2 (c)*** represents the ideal stoichiometric balance and exhibits the highest capacitive performance. The FESEM image reveals a dense, uniform distribution of BiOI nanoplates effectively intercalated within the MWCNT matrix. Here, the MWCNTs act as structural pillars that circumvent nanoplate restacking while simultaneously providing a continuous, low-resistance pathway for electron transport. This optimized morphology ensures maximum accessibility of electrolyte ions to the active facets and facilitates accelerated charge kinetics. Despite possessing a higher BiOI mass fraction in ***Figure 2 (d)*** than the optimized sample, a regression in capacitive performance is observed. The SEM reveals a more congested morphology of BiOI nanoplates and reduced ion-transport efficiency account for the diminished rate capability in this variant [48-50].

To verify the elemental composition and phase purity of the synthesized materials, EDAX measurements were performed, as presented in ***Figures 2(e–h)***. The EDAX spectrum of the pure BiOI sample confirms the presence of bismuth (Bi), oxygen (O), and iodine (I) as the primary constituents. The absence of extraneous peaks underscores the high purity of the synthesized nanoplates. For the nanocomposite variants, the emergence of a prominent carbon (C) peak, alongside the characteristic signals of Bi, O, and I, validates the successful hybridization of MWCNTs within the BiOI matrix. This elemental evidence confirms that the synthesis protocol successfully yielded high-purity nanocomposites with well-integrated

components, laying a robust foundation for the observed synergistic electrochemical performance.

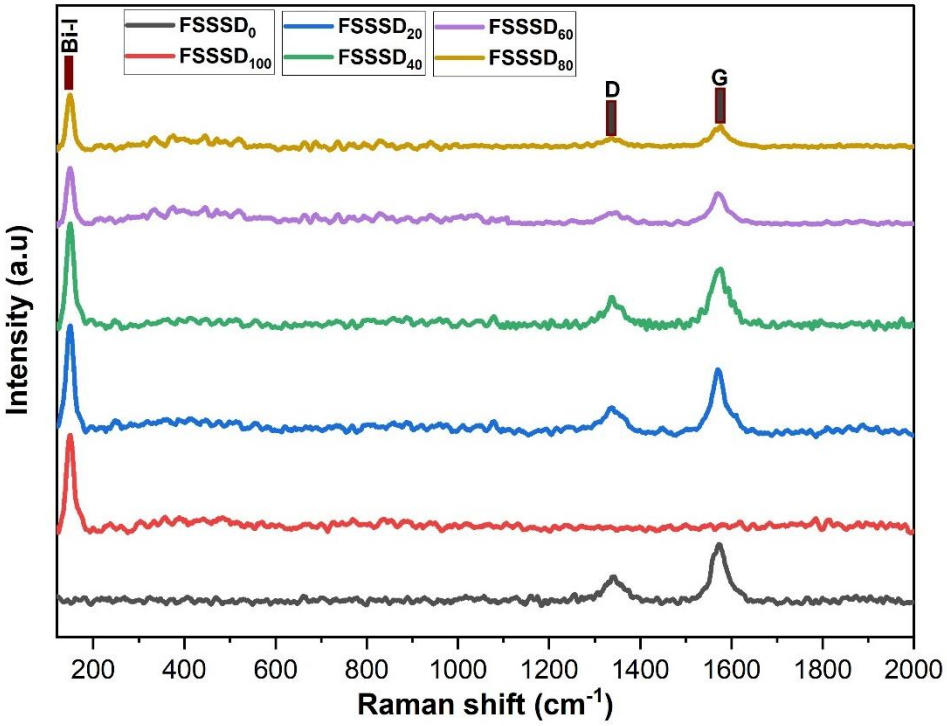


Figure 3: *Raman spectra of MWCNT($FSSSD_0$) Pure BiOI nanoplate ($FSSSD_{100}$) and BiOI/MWCNT nanocomposites ($FSSSD_{20}$, $FSSSD_{40}$, $FSSSD_{60}$,$FSSSD_{80}$)*

The Raman spectra for all samples are displayed in ***Figure 3***. The peak observed for BiOI/MWCNT nanocomposites ($FSSSD_{20\text{-}100}$) at 150 cm^{-1} corresponds to the A_{1g} stretching vibration of the Bi–I bond. Both pure MWCNT ($FSSSD_0$) and the BiOI/MWCNT(($FSSSD_{20\text{-}80}$) nanocomposites exhibit characteristic D and G bands at 1340 cm^{-1} and 1575 cm^{-1}, respectively [51-52]. The G band represents the in-plane vibrations of sp^2 bonded carbon atoms and serves as an indicator of graphitization, while the D band originates from out-of-plane vibrations associated with structural defects and broken symmetry within the graphite lattice [53-54].

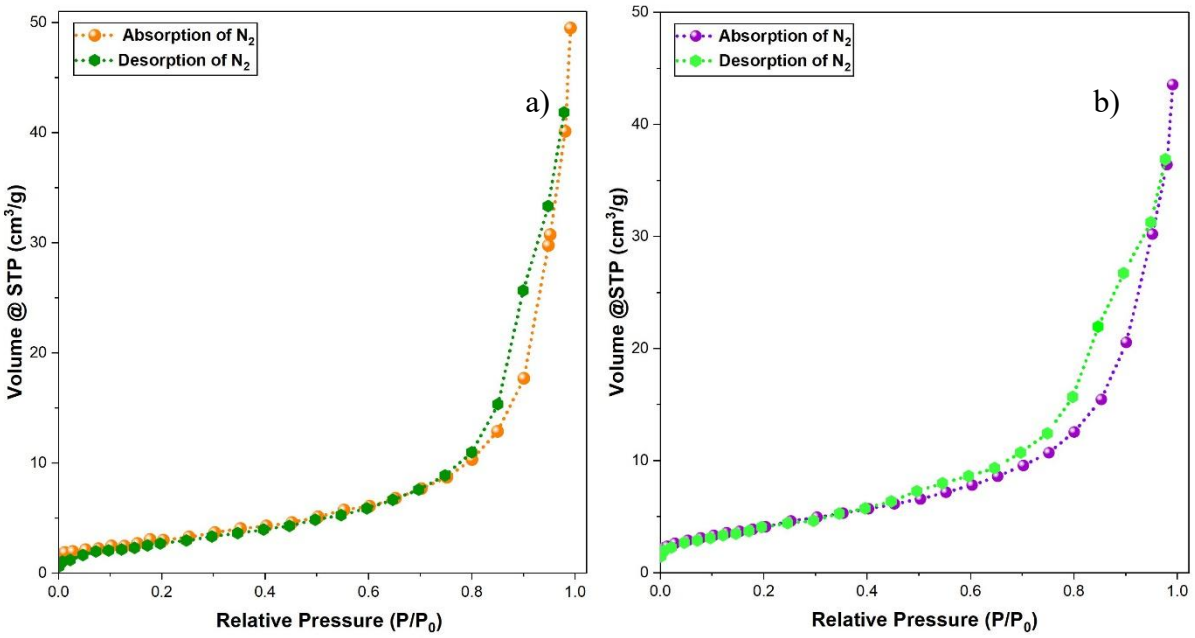


Figure 4: *N_2 adsorption-desorption isotherms (a) pure BiOI nanoplate and (b) BiOI/MWCNT ($FSSSD_{60}$) nanocomposites.*

To investigate the textural properties of the synthesized materials, N_2 adsorption–desorption isotherms were recorded [***Figure 4 (a-b***]. The observed Type-IV isotherms and H3-type hysteresis indicate that the samples possess a predominantly mesoporous architecture. In agreement with FESEM observations, the $FSSSD_{60}$ sample demonstrated superior textural properties, specifically yielding the higher specific surface area and pore volume as depicted in the supporting information (Figure. S1) [55-56].

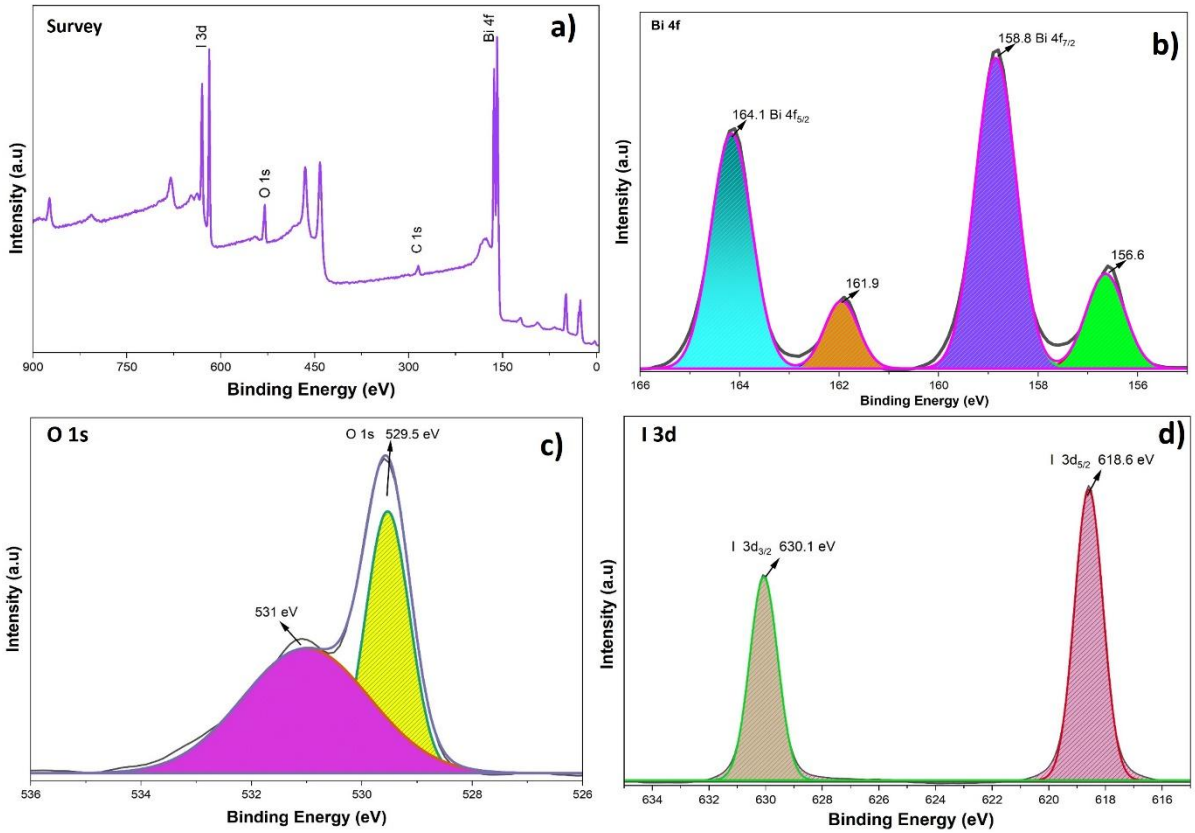


Figure 5*: XPS spectra of a) pure BiOI NP (survey spectra , b) Bi 4f , c) O 1s and d) I 3d*

The surface chemical composition and oxidation states of the synthesized BiOI nanoparticles were investigated by X-ray photoelectron spectroscopy (XPS) . The survey spectrum confirms the presence of Bi, O, and I elements without any detectable impurity peaks, indicating the high purity of the sample. A small C 1s peak observed at ~284.8 eV is attributed to adventitious carbon and was used as a reference for charge correction.

The high-resolution Bi 4f spectrum exhibits two prominent peaks located at approximately 158.8 eV and 164.1 eV, corresponding to Bi $4f_{7/2}$ and Bi $4f_{5/2}$, respectively (***Figure 5 b***). The spin–orbit splitting of about 5.3 eV confirms the presence of Bi in the +3 oxidation state. Additionally, characteristic Bi 4d peaks are observed in the range of ~441–466 eV, further supporting the formation of Bi^{3+} species in the lattice.

The O 1s spectrum (***Figure 5 a***) shows a peak centred around ~530 eV, which can be attributed to lattice oxygen (Bi–O bonding) in BiOI. A minor shoulder at slightly higher binding energy (~531 eV) may be associated with surface hydroxyl groups or adsorbed oxygen species.

The I 3d core level spectrum in ***Figure 5 (d)*** displays two distinct peaks at approximately 618.6 eV and 630.1 eV, corresponding to I $3d_{5/2}$ and I $3d_{3/2}$, respectively. The spin–orbit separation of nearly 11.5 eV is characteristic of iodide (I^-) species in BiOI.

Overall, the XPS results confirm the successful formation of stoichiometric BiOI with Bi^{3+}, O^{2-}, and I^- oxidation states, consistent with the expected chemical structure of bismuth oxyiodide [57-58].

4 Electrochemical analysis

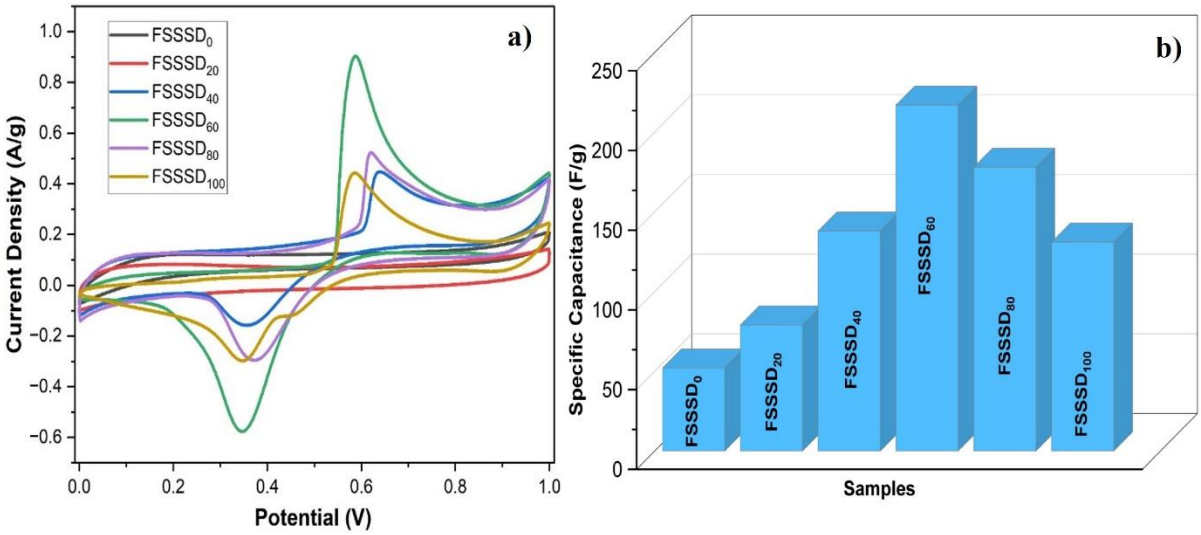


***Figure 6**: a) CV curves of pure BiOI/ MWCNT nanocomposites ($FSSSD_{0\text{-}100}$) samples at 5mV/s scan rate with PVA/H_2SO_4 gel electrolyte b) Specific capacitance of different $FSSSD_{0\text{-}100}$ samples*

To evaluate the electrochemical performance of the as-fabricated FSSSD devices across varying BiOI/MWCNT weight ratios, CV measurements were conducted within a 0 to 1 V potential window at a scan rate 5mV/s. As illustrated in ***Figure 6(a)***, the CV profiles at a scan rate 5mV/s indicate that the $FSSSD_{60}$ (60:40 BiOI/MWCNT) device achieves the highest specific capacitance. The calculated capacitance values for all devices graphically represented in ***Figure 6(b)***. This superior electrochemical behaviour is fundamentally linked to the optimized textural properties of the $FSSSD_{60}$ composite, which exhibits a BET surface area of 17.19 m^2g^{-1} and a pore volume of 0.062 cm^3g^{-1}. Such a porous architecture facilitates efficient electrolyte infiltration and maximizes the exposure of electroactive sites. Furthermore, the high intrinsic conductivity of the MWCNT network ensures rapid charge transport, justifying the selection of the 60:40 composite for subsequent electrochemical investigations [59-60].

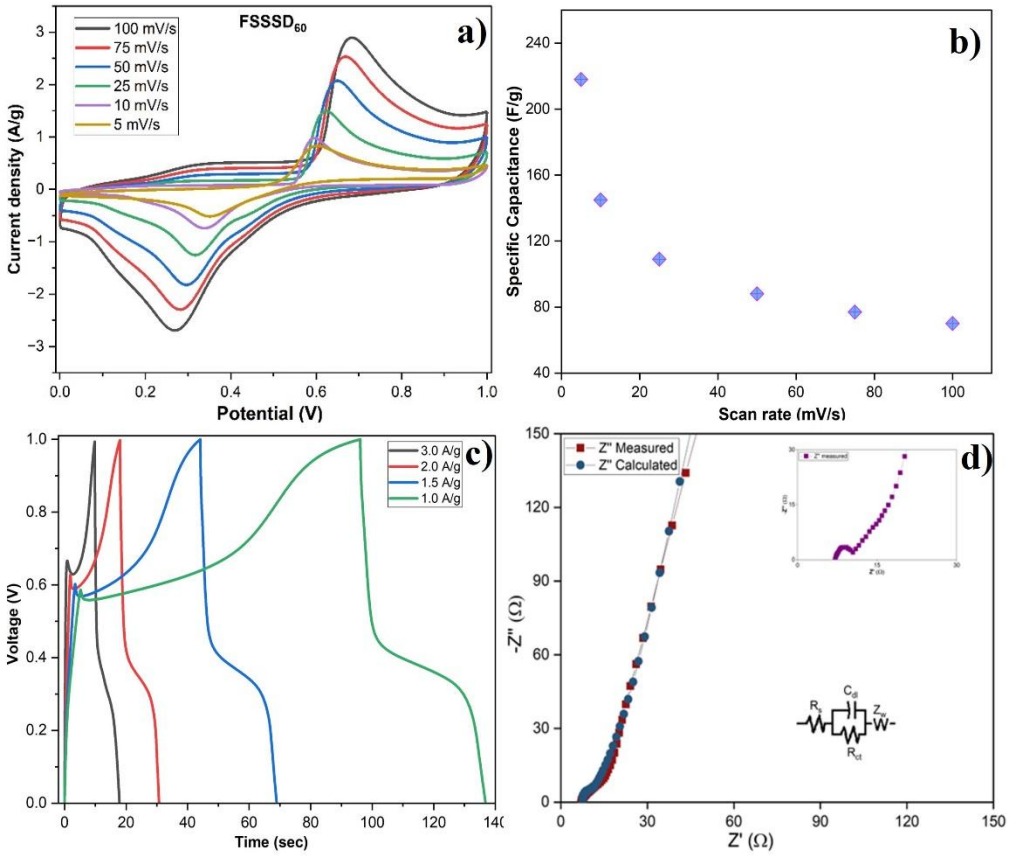


Figure 6: ***a)*** *CV curves of $FSSSD_{60}$ nanocomposite at different scan rates with PVA/ H_2SO_4 gel electrolyte b) Variation of Specific capacitance with different scan rates, c) GCD curves of $FSSSD_{60}$ at different current densities and (d) Nyquist plot with equivalent circuit.*

Based on the preliminary results, the $FSSSD_{60}$ device was selected for comprehensive electrochemical evaluation. ***Figures 7(a)*** and ***7(c)*** illustrate the CV and GCD profiles of $FSSSD_{60}$ across various scan rates and current densities, respectively. The specific capacitance values derived from the CV curves were 218, 145, 109, 88, 77 and 70 F/g at scan rates of 5, 10, 25, 50, 75 and 100 mV/s, respectively which is shown graphically in ***Figure 7 (b)*** [61-62]. The electrochemical energy storage mechanism of BiOI is governed by the following redox reaction:

$$BiOI + H_2O + 3e \rightarrow Bi + I^- + 2OH^- \qquad (i)$$

$$2Bi + 6OH \leftrightarrow Bi_2O_3 + 3H_2O + 6e^- \qquad (ii)$$

To further investigate the interfacial kinetics and charge transport mechanisms of the synthesized electrode, electrochemical impedance spectroscopy (EIS) was performed. ***Figure***

7(d) displays the Nyquist plot, which consists of a high-frequency semicircle followed by a prominent linear tail in the low-frequency region.

The experimental data were fitted using the modified Randles equivalent circuit model: R_s (C_{dl} Rct) Z_w. The circuit parameters, including the solution resistance (R_s), double-layer capacitance (C_{dl}), charge transfer resistance (R_{ct}), and Warburg impedance (Z_w), were extracted [63-64]. The internal resistance (R_s) was found to be 7.11 Ω, reflecting the cumulative resistance of the electrolyte and the intrinsic conductivity of the active material. The double layer capacitance (C_{dl}) was calculated as 12.83 μF which characterizes the non faradic charge accumulation at the electrode electrolyte interfaces and it is directly influenced by the effective surface area of the nanocomposite materials accessible to the ions. Notably, the charge transfer resistance (R_{ct}) is low 3.34 Ω , indicating near-instantaneous electron transfer at the electrode-electrolyte interface [65-66]. This suggests that the incorporation of MWCNTs significantly enhances the electroactive surface area and conductivity.

In the low-frequency region, the system is dominated by the Warburg impedance (Z_w), the linear trend observed indicates a diffusion-controlled process, characteristic of ion transport within the porous architecture of the nanocomposite. The high slope of this diffusion tail signifies favorable capacitive behaviour with efficient ion accessibility [67-68].

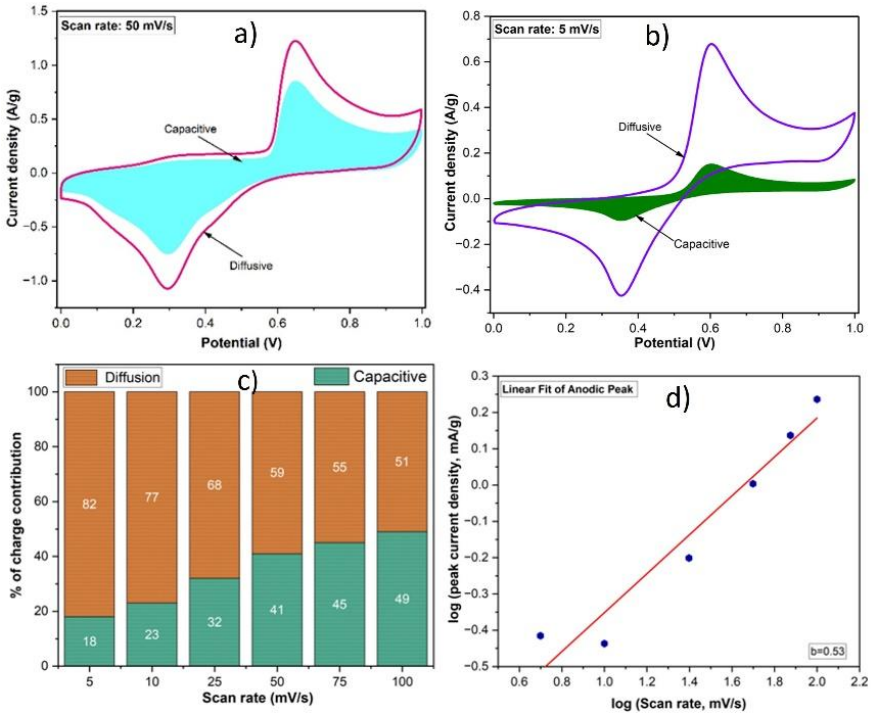


***Figure 7**: a) comparison of diffusive and capacitive contribution at scan rate 50 mV/s, b) comparison of diffusive and capacitive contribution at 5 mV/s c) Scan rate vs percentage of charge contribution at different scan rate (d) log (i_p) vs log(v) graph*

The charge storage mechanism of the electrode was systematically investigated to differentiate between surface-controlled (capacitive) and diffusion-controlled (intercalation/battery-type) processes. This distinction is vital for determining the suitability of the material for high-power supercapacitor applications.

The relationship between the peak current (i) and the scan rate (av^b) provides a fundamental indicator of the kinetic regime. This is expressed by the power-law equation [69]:

$$i = av^b$$

Taking the logarithm of both sides yields:

$$\log(i) = b \log(v) + \log(a)$$

As illustrated in ***Figure 8 (d)***, the plot of $\log(i)$ versus $\log(v)$ for the anodic peak shows a linear fit with a slope of b = 0.53. A b value of 0.5 indicates a purely diffusion-controlled process, characteristic of faradaic intercalation. Conversely, a b value of 1.0 indicates a capacitive process. The calculated value of 0.53 suggests that the electrode exhibits a battery-like behaviour where ion diffusion into the bulk of the material is the primary current-limiting

step [70-72]. However, the slight deviation toward higher values implies the presence of pseudocapacitive surface effects, which are likely enhanced by the integration of the MWCNT network.

To further isolate the specific contributions at various potentials, we utilized the method proposed by Dunn et al., which partitions the total current $i(\mathrm{V})$ at a specific potential V

$$i(\mathrm{V}) = k_1 v + k_2 v^{1/2}$$

Here, $k_1 v$ represents the current contribution from capacitive effects (surface-controlled), and $k_2 v^{1/2}$represents the current from diffusion-controlled processes. By plotting $i(\mathrm{V})/v^{1/2}$ against $v^{1/2}$, the slopes and intercepts provide the values for k_1 and k_2 at each potential point. **Figures 8 (a) and (b)** show the deconvolution results at 50 mV/s and 5 mV/s, respectively. At 5 mV/s, the diffusion-controlled current dominates, covering the majority of the CV area. This is due to the extended time scales allowing for deep penetration of electrolyte ions into the BiOI nanosheets. At 50 mV/s, the capacitive contribution (Figure 8(a), cyan area) increases significantly. This highlights the material's ability to store charge rapidly via surface adsorption and fast surface redox reactions, even when the bulk diffusion is kinetically limited by the fast scan rate [73].

The bar chart in ***Figure 8(c)*** summarizes the quantitative ratio of these two mechanisms. At a low scan rate of 5 mV/s, the diffusion contribution is 82%, reflecting the high capacity intrinsic to the material's bulk structure. As the scan rate increases to 100 mV/s, the capacitive contribution rises to 49%. The significant rise in capacitive percentage at high scan rates is a testament to the synergistic effect between the active BiOI and the highly conductive MWCNT scaffold. The MWCNTs facilitate rapid electron transport and provide a high surface area for electrolyte ion accessibility. This ensures that the electrode maintains high power density and rate capability, which are essential requirements for the development of flexible, high-performance supercapacitors.

The kinetic behavior observed in the CV analysis correlates strongly with the material's structural features. The mesoporous nature confirmed via BET analysis and the hierarchical arrangement of the nanocomposite allow for a high degree of electrolyte exposure. The small b value 0.53 indicates that the bulk material is fully utilized at low speeds, maximizing energy density. The near-equal split between capacitive and diffusive processes at 100 mV/s indicates

that the electrode does not suffer from extreme ohmic drops or kinetic bottlenecks, which is often a failure point in thicker or less conductive electrode designs. These findings confirm that the composite is a promising candidate for next-generation flexible energy storage systems

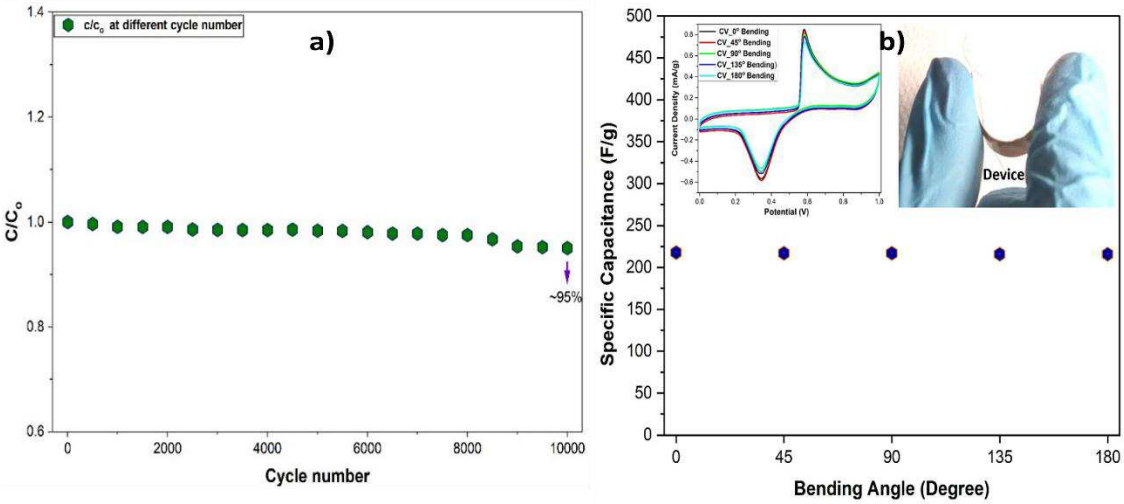


Figure 9*: a) Cycle stability curve (b) Specific capacitance vs bending angle graph of FSSSD$_{60}$, inset figure left corner shows CV curves at different bending conditions for FSSSD$_{60}$ flexible electrode at scan rate 5mV/s and flexible electrode (inset figure right corner)*

The FSSSC$_{60}$ device also demonstrated remarkable cyclic stability, retaining 95% of its initial capacitance after 10,000 cycles (***Figure 9(a)***). SEM imaging following electrochemical cycling revealed no significant alterations in morphology or crystallinity, validating the electrode's structural robustness (Figure. S2). The specific capacitance remains almost constant across various bending angle, highlighting the excellent structural stability of the flexible supercapacitor which is shown in ***Figure 9(b).***

5 Conclusion:

In summary, this work successfully demonstrates the fabrication of a high-performance, flexible solid-state symmetric supercapacitor device (FSSSD) based on 2D-BiOI nanoplate/MWCNT nanocomposites. Systematic investigation of varying weight ratios revealed that the FSSSD$_{60}$ (60:40 wt%) composition serves as the optimal electrode material, delivering a superior specific capacitance of 218 F/g and a high energy density of 7.6 Wh/kg at a power density of 0.136 W/kg. These enhanced electrochemical properties are intrinsically linked to the material's optimized textural parameters, specifically a BET surface area of

17.190 m^2g^{-1} and a pore diameter 15 nm. This porous architecture facilitates efficient electrolyte infiltration and maximizes the exposure of electroactive sites, while the conducting network of MWCNTs ensures rapid charge-transport kinetics. Furthermore, the $FSSSD_{60}$ device exhibited remarkable long-term durability, retaining 95% of its initial capacitance after 10,000 charge-discharge cycles. Post-cycling FESEM analyses confirmed that the electrode maintains its morphological and crystallographic integrity, validating its structural robustness. The device also demonstrated exceptional mechanical flexibility, maintaining stable capacitive performance under various bending angles. These findings underscore the potential of BiOI/MWCNT nanocomposites as a viable and efficient electrode material for next-generation flexible and wearable energy storage systems.

Acknowledgement

This study was supported by the Ramanujan Fellowship (SR/S2/RJN 98/2011), DST-FIST (SR/FST/PSI-188/2013) of the Department of Science and Technology (DST), Government of India. The authors also express their gratitude to the UGC-DAE CSR, Kolkata Centre, for financial support (UGC-DAE-CSR-KC/CRS/19/MS08/0933/0972). The authors would like to thank IIT Delhi, Sonipat Campus, for their assistance with BET and XPS measurements.

References

[1] P. S. Babu *et al.*, "Solvothermal synthesis and electrochemical performance of BiOBr nanosheets for symmetric supercapacitor devices," *Scientific Reports*, vol. 15, no. 1, p. 45787, 2025.

[2] "Ramasamy, B., Manoharan, K., Raman, K. & Sundaram, R. Blooming flower-like BiOBr decorated RGO nanocomposite as an advanced electrode material for high-performance supercapattery applications. Mater. Sci. Eng. B 300, 117108 (2024).".

[3] "Devi, N. & Ray, S. S. Performance of bismuth-based materials for supercapacitor applications: A review. Mater. Today Commun. 25, 101691 (2020).".

[4] E. Frackowiak, "Carbon materials for supercapacitor application," *Physical chemistry chemical physics*, vol. 9, no. 15, pp. 1774–1785, 2007.

[5] S. Park and S. Jayaraman, "Smart textiles: Wearable electronic systems," *MRS bulletin*, vol. 28, no. 8, pp. 585–591, 2003.

[6] Z. Fang, C. Peng, Q. Zhou, and Z. Liu, "Electrocatalytic hydrogen peroxide production: advances, challenges, and future perspectives," *The Chemical Record*, vol. 25, no. 9, p. e202500066, 2025.

[7] L. Liu, Y. Yu, C. Yan, K. Li, and Z. Zheng, "Wearable energy-dense and power-dense supercapacitor yarns enabled by scalable graphene–metallic textile composite electrodes," *Nature communications*, vol. 6, no. 1, p. 7260, 2015.

[8] R. Ramesh, "Review of battery-supercapacitor hybrid energy storage systems for electric vehicles," *Results in Engineering*, vol. 24, p. 103598, 2024.

[9] X. Xu *et al.*, "Challenges and opportunities toward long-life lithium-ion batteries," *Journal of Power Sources*, vol. 603, p. 234445, 2024.

[10] S. Huang, X. Zhu, S. Sarkar, and Y. Zhao, "Challenges and opportunities for supercapacitors," *APL materials*, vol. 7, no. 10, 2019.

[11] J. P. Baboo *et al.*, "Investigating battery-supercapacitor material hybrid configurations in energy storage device cycling at 0.1 to 10C rate," *Journal of power sources*, vol. 561, p. 232762, 2023.
[12] J. Libich, J. Máca, J. Vondrák, O. Čech, and M. Sedlaříková, "Supercapacitors: Properties and applications," *Journal of energy storage*, vol. 17, pp. 224–227, 2018.
[13] C. Lekakou, O. Moudam, F. Markoulidis, T. Andrews, J. F. Watts, and G. T. Reed, "Carbon-based fibrous EDLC capacitors and supercapacitors," *Journal of Nanotechnology*, vol. 2011, no. 1, p. 409382, 2011.
[14] S. Q. Zheng *et al.*, "Advances in Design and Application of Nanostructured TMOs and Their Composites for High-Performance Supercapacitors," *Handbook of Energy Materials in Supercapacitors and Storage Devices*, pp. 255–294, 2026.
[15] S. Ghosh, S. R. Polaki, A. Macrelli, C. S. Casari, S. Barg, and S. M. Jeong, "Nanoparticle-enhanced Multifunctional Nanocarbons as Metal-ion Battery and Capacitor Anodes and Supercapacitor Electrodes--Review," *arXiv preprint arXiv:2201.12463*, 2022.
[16] J. Peng, Z. Chen, B. Ding, and H.-M. Cheng, "Recent advances for the synthesis and applications of 2-dimensional ternary layered materials," *Research*, vol. 6, p. 0040, 2023.
[17] I. Ahmed and A. Majid, "Harnessing chromium oxychloride for next-generation monovalent and multivalent ion batteries: First principles investigations," *Materials Science in Semiconductor Processing*, vol. 192, p. 109413, 2025.
[18] X. Wang *et al.*, "All-solid-state fiber-shaped asymmetric supercapacitors with ultrahigh energy density based on porous vanadium nitride nanowires and ultrathin Ni (OH) 2 nanosheet wrapped NiCo2O4 nanowires arrays electrode," *The Journal of Physical Chemistry C*, vol. 123, no. 2, pp. 985–993, 2018.
[19] B. Wei, F. Ming, H. Liang, Z. Qi, W. Hu, and Z. Wang, "All nitride asymmetric supercapacitors of niobium titanium nitride-vanadium nitride," *Journal of Power Sources*, vol. 481, p. 228842, 2021.
[20] A. Ammasi, A. P. Munusamy, M. Shkir, B. Vellingiri, V. R. M. Reddy, and W. K. Kim, "Design and fabrication of BaSnO3/RGO as efficient Pt-free counter electrode for dye-sensitized solar cells," *Journal of Materials Science: Materials in Electronics*, vol. 34, no. 32, p. 2168, 2023.
[21] S. Sahoo, G. Dhakal, W. Kim, and J. Shim, "Ternary Nanohybrid of Ni3S2/CoMoS4/MnO2 on Nickel Foam for Aqueous and Solid-State High-Performance Supercapacitors. Nanomaterials 2022, 12, 1945," *ed: s Note: MDPI stays neutral with regard to jurisdictional claims in published*, 2022.
[22] H. R. Ghenaatian, M. F. Mousavi, and M. S. Rahmanifar, "High performance hybrid supercapacitor based on two nanostructured conducting polymers: Self-doped polyaniline and polypyrrole nanofibers," *Electrochimica acta*, vol. 78, pp. 212–222, 2012.
[23] M. Xu, T. Liang, M. Shi, and H. Chen, "Graphene-like two-dimensional materials," *Chemical reviews*, vol. 113, no. 5, pp. 3766–3798, 2013.
[24] P. Miró, M. Audiffred, and T. Heine, "An atlas of two-dimensional materials," *Chemical Society Reviews*, vol. 43, no. 18, pp. 6537–6554, 2014.
[25] J. Liu, H. Cao, B. Jiang, Y. Xue, and L. Fu, "Newborn 2D materials for flexible energy conversion and storage," *Science China Materials*, vol. 59, no. 6, pp. 459–474, 2016.
[26] F. Bonaccorso *et al.*, "Graphene, related two-dimensional crystals, and hybrid systems for energy conversion and storage," *Science*, vol. 347, no. 6217, p. 1246501, 2015.
[27] M. A. H. C. Anik *et al.*, "Hierarchical integration of a MoS 2 nanoflower/MnO 2 nanorod/CNT ternary composite electrode for high capacitance and long-term cycling stability," *Materials Advances*, vol. 6, no. 24, pp. 9723–9745, 2025.

[28] R. Amin, P. R. Kumar, and I. Belharouak, “Carbon nanotubes: Applications to energy storage devices,” *Carbon Nanotubes-Redefining the World of Electronics*, vol. 10, pp. 5772–94155, 2020.
[29] T. Brousse, D. Bélanger, and J. W. Long, “To be or not to be pseudocapacitive?,” *Journal of The Electrochemical Society*, vol. 162, no. 5, pp. A5185–A5189, 2015.
[30] M. Beidaghi and Y. Gogotsi, “Capacitive energy storage in micro-scale devices: recent advances in design and fabrication of micro-supercapacitors,” *Energy & Environmental Science*, vol. 7, no. 3, pp. 867–884, 2014.
[31] Y. Zhu *et al.*, “Carbon-based supercapacitors produced by activation of graphene,” *science*, vol. 332, no. 6037, pp. 1537–1541, 2011.
[32] Y. Shao *et al.*, “Graphene-based materials for flexible supercapacitors,” *Chemical Society Reviews*, vol. 44, no. 11, pp. 3639–3665, 2015.
[33] H. Choi and H. Yoon, “Nanostructured electrode materials for electrochemical capacitor applications,” *Nanomaterials*, vol. 5, no. 2, pp. 906–936, 2015.
[34] H. Zhu *et al.*, “Nanocomposites of conducting polymers and 2D materials for flexible supercapacitors,” *Polymers*, vol. 16, no. 6, p. 756, 2024.
[35] “Hegazy HH, Khan J, Shakeel N, Alabdullkarem EA, Saleem MI, Alrobei H, Yahia IS. 2D-based electrode materials for supercapacitors–status, challenges, and prospects. RSC advances. 2024;14(45):32958-77.”.
[36] “Yan Z, Luo S, Li Q, Wu ZS, Liu S. Recent advances in flexible wearable supercapacitors: properties, fabrication, and applications. Advanced Science. 2024 Feb;11(8):2302172.”.
[37] “Yang D, Xu P, Tian C, Li S, Xing T, Li Z, Wang X, Dai P. Biomass-derived flexible carbon architectures as self-supporting electrodes for energy storage. Molecules. 2023 Aug 31;28(17):6377.”.
[38] “Patil DS, Shaikh JS, Dalavi DS, Kalagi SS, Patil PS. Chemical synthesis of highly stable PVA/PANI films for supercapacitor application. Materials Chemistry and Physics. 2011 Aug 15;128(3):449-55.”.
[39] “Zhu H, Xu R, Wan T, Yuan W, Shu K, Boonprakob N, Zhao C. Nanocomposites of conducting polymers and 2D materials for flexible supercapacitors. Polymers. 2024 Mar 9;16(6):756.”.
[40] “The synthesis of single-crystal BiOI nanoplates with {001} facets exposed Da Zhang1, 2, a*, Liang Chen1, 2, b, Tao Wei1, 2, c, Chengjing Xiao1, 2, d and Zaiqin Wang2, 3, e”.
[41] “Indium doped BiOI nanosheets: Preparation, characterization and photocatalytic degradation activity Authors: Haibo Li, Zujin Yang, Jingnan Zhang, Yongchao Huang, Hongbing Ji, Yexiang Tong”.
[42] “E.M. Doherty, S. De, P.E. Lyons, A. Shmeliov, P.N. Nirmalraj, V. Scardaci. J. Joimel, W.J. Blau, J.J. Boland, J.N. Coleman, The spatial uniformity and electromechanical stability of transparent, conductive films of single walled nanotubes, Carbon. 47 (2009) 2466-2473.”.
[43] W. Zeng *et al.*, “Synthesis of large-area atomically thin BiOI crystals with highly sensitive and controllable photodetection,” *Advanced Functional Materials*, vol. 29, no. 16, p. 1900129, 2019.
[44] I. D. Sharma, I. D. Sharma, C. Kant, A. K. Sharma, R. R. Pandey, and K. K. Saini, “A Simple Route to Synthesize Nanostructures of Bismuth Oxyiodide and Bismuth Oxychloride (BiOI/BiOCl) Composite for Solar Energy Harvesting,” *Trends and Applications in Advanced Polymeric Materials*, pp. 83–100, 2017.

[45] X. Zhang, Z. Ai, F. Jia, and L. Zhang, “Generalized one-pot synthesis, characterization, and photocatalytic activity of hierarchical BiOX (X= Cl, Br, I) nanoplate microspheres,” *The Journal of Physical Chemistry C*, vol. 112, no. 3, pp. 747–753, 2008.
[46] L. Zhang, A. A. Gonçalves, and M. Jaroniec, “Identification of preferentially exposed crystal facets by X-ray diffraction,” *RSC advances*, vol. 10, no. 10, pp. 5585–5589, 2020.
[47] I. Kazeminezhad, N. Hekmat, and A. Kiasat, “Effect of growth parameters on structural and optical properties of CdS nanowires prepared by polymer controlled solvothermal route,” *Fibers and Polymers*, vol. 15, no. 4, pp. 672–679, 2014.
[48] M. E. Kazyrevich, M. V. Malashchonak, A. V. Mazanik, E. A. Streltsov, A. I. Kulak, and C. Bhattacharya, “Photocurrent switching effect on platelet-like BiOI electrodes: influence of redox system, light wavelength and thermal treatment,” *Electrochimica Acta*, vol. 190, pp. 612–619, 2016.
[49] M. Su *et al.*, “Enhanced adsorption and photocatalytic activity of BiOI–MWCNT composites towards organic pollutants in aqueous solution,” *Journal of hazardous materials*, vol. 229, pp. 72–82, 2012.
[50] Y. Li *et al.*, “Multi-walled carbon nanotubes/BiPO4/BiOI heterostructure composite photoelectrochemical sensor in detection of salicylic acid,” *Journal of The Electrochemical Society*, vol. 167, no. 6, p. 066521, 2020.
[51] N. Sharma *et al.*, “Combination of iodine-deficient BiOI phases in the presence of CNT to enhance photocatalytic activity towards phenol decomposition under visible light,” *Applied Surface Science*, vol. 565, p. 150605, 2021.
[52] E. F. Antunes, A. O. Lobo, E. J. Corat, V. J. Trava-Airoldi, A. A. Martin, and C. Veríssimo, “Comparative study of first-and second-order Raman spectra of MWCNT at visible and infrared laser excitation,” *Carbon*, vol. 44, no. 11, pp. 2202–2211, 2006.
[53] A. Gupta, S. R. Dhakate, P. Pal, A. Dey, P. K. Iyer, and D. K. Singh, “Effect of graphitization temperature on structure and electrical conductivity of poly-acrylonitrile based carbon fibers,” *Diamond and Related Materials*, vol. 78, pp. 31–38, 2017.
[54] M. Acik *et al.*, “Spectroscopic evaluation of out-of-plane surface vibration bands from surface functionalization of graphite oxide by fluorination,” *Carbon*, vol. 77, pp. 577–591, 2014.
[55] D. Feng *et al.*, “Multi-layered mesoporous TiO 2 thin films with large pores and highly crystalline frameworks for efficient photoelectrochemical conversion,” *Journal of Materials Chemistry A*, vol. 1, no. 5, pp. 1591–1599, 2013.
[56] B. Freitas *et al.*, “Robust, flexible, freestanding and high surface area activated carbon and multi-walled carbon nanotubes composite material with outstanding electrode properties for aqueous-based supercapacitors,” *Materials Advances*, vol. 2, no. 13, pp. 4264–4276, 2021.
[57] V. Mahmoodi, A. Ahmadpour, T. Rohani Bastami, and M. T. Hamed Mousavian, “Facile synthesis of BiOI nanoparticles at room temperature and evaluation of their photoactivity under sunlight irradiation,” *Photochemistry and Photobiology*, vol. 94, no. 1, pp. 4–16, 2018.
[58] S. Asadzadeh-Khaneghah, A. Habibi-Yangjeh, and D. Seifzadeh, “Graphitic carbon nitride nanosheets coupled with carbon dots and BiOI nanoparticles: boosting visible-light-driven photocatalytic activity,” *Journal of the Taiwan Institute of Chemical Engineers*, vol. 87, pp. 98–111, 2018.
[59] R. H. Baughman, A. A. Zakhidov, and W. A. De Heer, “Carbon nanotubes--the route toward applications,” *science*, vol. 297, no. 5582, pp. 787–792, 2002.
[60] “Y.-K. Hsu, Y.-C. Chen, Y.-G. Lin, Synthesis of copper sulfide nanowire arrays for high-performance supercapacitors, Electrochimica Acta 139 (2014) 401–407.”.

[61] A. Ramadoss, K.-Y. Yoon, M.-J. Kwak, S.-I. Kim, S.-T. Ryu, and J.-H. Jang, “Fully flexible, lightweight, high performance all-solid-state supercapacitor based on 3-Dimensional-graphene/graphite-paper,” *Journal of Power Sources*, vol. 337, pp. 159–165, 2017.
[62] S. Zhang, B. Yin, Z. Wang, and F. Peter, “Super long-life all solid-state asymmetric supercapacitor based on NiO nanosheets and α-Fe2O3 nanorods,” *Chemical Engineering Journal*, vol. 306, pp. 193–203, 2016.
[63] G. A. Ruiz and C. J. Felice, “Electrochemical-fractal model versus randles model: A discussion about diffusion process,” *International Journal of Electrochemical Science*, vol. 10, no. 10, pp. 8484–8496, 2015.
[64] E. Rahmawati, D. R. Santoso, J. A. F. Noor, and A. Nadhir, “Electrical impedance analysis of NaCl and CaCl2 solutions based on equivalent electric circuit,” in *Journal of Physics: Conference Series*, IOP Publishing, 2022, p. 012025.
[65] M. Catelani *et al.*, “Experimental characterization of hybrid supercapacitor under different operating conditions using EIS measurements,” *IEEE Transactions on Instrumentation and Measurement*, vol. 73, pp. 1–10, 2023.
[66] M. Y. Perdana *et al.*, “Understanding the behavior of supercapacitor materials via electrochemical impedance spectroscopy: a review,” *The Chemical Record*, vol. 24, no. 5, p. e202400007, 2024.
[67] S. Karmakar, “Impedance spectroscopy for electroceramics and electrochemical system,” *arXiv preprint arXiv:2406.15467*, 2024.
[68] J. E. Craven, D. S. Kinnamon, and S. Prasad, “Randles circuit analysis toward investigating interfacial effects on microchannel electrodes,” *IEEE Sensors Letters*, vol. 2, no. 1, pp. 1–4, 2018.
[69] J. Liu *et al.*, “Advanced energy storage devices: basic principles, analytical methods, and rational materials design,” *Advanced science*, vol. 5, no. 1, p. 1700322, 2018.
[70] V. Augustyn *et al.*, “High-rate electrochemical energy storage through Li+ intercalation pseudocapacitance,” *Nature materials*, vol. 12, no. 6, pp. 518–522, 2013.
[71] J. Come, P.-L. Taberna, S. Hamelet, C. Masquelier, and P. Simon, “Electrochemical kinetic study of LiFePO4 using cavity microelectrode,” *Journal of The Electrochemical Society*, vol. 158, no. 10, pp. A1090–A1093, 2011.
[72] J. Wang, J. Polleux, J. Lim, and B. Dunn, “Pseudocapacitive contributions to electrochemical energy storage in TiO2 (anatase) nanoparticles,” *The Journal of Physical Chemistry C*, vol. 111, no. 40, pp. 14925–14931, 2007.
[73] M. Sathiya, A. S. Prakash, K. Ramesha, J.-M. Tarascon, and A. K. Shukla, “V2O5-anchored carbon nanotubes for enhanced electrochemical energy storage,” *Journal of the American Chemical Society*, vol. 133, no. 40, pp. 16291–16299, 2011.

Supplementary Files

This is a list of supplementary files associated with this preprint. Click to download.

- SupportingFileSep2026.docx